

## PAPER



Cite this: *Phys. Chem. Chem. Phys.*,  
2014, 16, 23431

## Enhanced photoelectrochemical performance by synthesizing CdS decorated reduced TiO<sub>2</sub> nanotube arrays†

Qian Zhang,<sup>a</sup> Ling Wang,<sup>a</sup> Jiangtao Feng,<sup>a</sup> Hao Xu<sup>\*a</sup> and Wei Yan<sup>\*ab</sup>

The efficient utilization of solar spectrum and photo-induced charge transport are critical aspects in improving the light conversion efficiency of solar cells and hydrogen generation. In this work, reduced TiO<sub>2</sub> nanotube arrays with CdS decoration were fabricated through the simple cathodic polarization of annealed TiO<sub>2</sub> nanotube arrays followed by the chemical deposition of CdS nanoparticles. Scanning electron microscopy (SEM), X-ray diffraction (XRD) and Raman spectroscopy confirmed the successful fabrication of the target material. UV-visible diffuse reflectance spectra showed a Burstein–Moss shift for reduced TiO<sub>2</sub> NTs and a red shift of the absorption edge towards ca. 563 nm for CdS-decorated R-TiO<sub>2</sub> NTs. Cyclic voltammetry and impedance spectra together demonstrate the decreased charge transport resistance for reduced TiO<sub>2</sub> NTs. Under the excitation of monochromatic light at 420 nm, the proposed CdS-decorated reduced TiO<sub>2</sub> NTs exhibit the maximum IPCE value of 30.12% in 1 M Na<sub>2</sub>SO<sub>3</sub> electrolyte, which is almost twice higher than that achieved on CdS-decorated pristine TiO<sub>2</sub> NTs. Therefore, the results here highlight the significance of charge transport in the light conversion process. The enhanced charge transport properties are ascribed to the increased number of electrons, which is brought about by the lattice oxygen vacancies (Ti<sup>3+</sup>) during the cathodic polarization.

Received 7th July 2014,  
Accepted 15th September 2014

DOI: 10.1039/c4cp02967d

www.rsc.org/pccp

## Introduction

Ever-increasing worldwide energy demand and environmental deterioration issues have induced the exploitation of clean energy sources such as solar energy. Such an intermittent form of energy can be captured and transformed over semiconductors into electricity or hydrogen to meet the requirements of a stable energy source for human lives and economic development. Therefore, studies on efficient, abundant and stable semiconductors for solar conversion are attracting increasing interest worldwide. Since the first time that Fujishima and Honda discovered the remarkable water splitting phenomenon on a TiO<sub>2</sub> photoanode, the attempt to explore and enhance the photoelectrochemical activity of TiO<sub>2</sub> has never stopped.<sup>1</sup> This is essentially ascribed to the promising features of TiO<sub>2</sub> such

as easy fabrication, thermo-chemical stability and reasonably high incident light-to-current generation. Nevertheless, the poor bulk conductivity and the slow charge mobility, as well as the inferior optical absorption range (<387 nm), restrict its further practical use.<sup>2</sup>

In recent years, highly ordered TiO<sub>2</sub> nanotube arrays (TiO<sub>2</sub> NTs) have attracted tremendous interest owing to their excellent light scattering and charge transport properties.<sup>3–5</sup> However, several studies have claimed that the electron transport still follows the multiple-trapping mode, which is similar to the charge transport fashion in disordered nanoparticle networks.<sup>6–8</sup> This is attributed to the presence of sub-band gap states in polycrystalline TiO<sub>2</sub> NTs, which increases the chances of electron scattering.<sup>7,8</sup> The cyclic voltammograms of nanoporous TiO<sub>2</sub> evidence the exponential distribution of these localized sub-band gap states below the conduction band, whereas the chemical origins and spatial location still remain unclear.<sup>9</sup> Through time-resolved terahertz spectroscopy, Christiaan Richter *et al.* revealed that the sluggish electron mobility in TiO<sub>2</sub> NTs results from the incomplete Ti coordination (Ti<sup>3+</sup>) sites.<sup>6</sup> Thus, improved electron mobility in TiO<sub>2</sub> NTs is suggested by the removal of such Ti<sup>3+</sup> states.

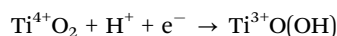
It is indeed the case that the presence of Ti<sup>3+</sup> defects could cause electron scattering and decreased mobility, whereas the benefit of Ti<sup>3+</sup> defects, namely the enhanced electrical conductivity, has also been raised.<sup>10,11</sup> It is believed that Ti<sup>3+</sup>-induced

<sup>a</sup> Department of Environmental Science and Engineering, Xi'an Jiaotong University, Xi'an, 710049, China. E-mail: xuhao@mail.xjtu.edu.cn, yanwei@mail.xjtu.edu.cn; Tel: +86 029 82664731

<sup>b</sup> The State Key Laboratory of Multiphase Flow in Power Engineering, Xi'an Jiaotong University, Xi'an, 710049, China

† Electronic supplementary information (ESI) available: The XPS survey spectrum of the composite CdS/R-TiO<sub>2</sub> NTs material is shown in Fig. S1. The impedance equivalent circuits used to fit the Nyquist plots are shown in Fig. S2. The photoactivity comparison between pristine TiO<sub>2</sub> NTs and reduced TiO<sub>2</sub> NTs for the decomposition of salicylic acid is shown in Fig. S3. See DOI: 10.1039/c4cp02967d

midgap states, as shallow donor sites, could contribute to the charge density enhancement and band gap narrowing, and lead to further improved photoelectrochemical efficiency.<sup>10,12</sup> In this regard, several strategies have been put forward to introduce oxygen vacancies (the cause for  $\text{Ti}^{3+}$  species) into the  $\text{TiO}_2$  lattice, including vacuum annealing, hydrogenation, electrochemical doping, high energy bombardment and chemical reduction with  $\text{NaBH}_4$ .<sup>10,13,14</sup> Among these approaches, electrochemical doping *via* cathodic polarization is a facile and accurate method, requiring neither harsh conditions nor troublesome operation. According to previous studies on  $\text{TiO}_2$ , the charge carrier density is strongly dependent on the external potential.<sup>15</sup> By subjecting them to a strong negative bias,  $\text{TiO}_2$  films would show a great enhancement on capacitance and electrical conductivity. The following equation presents the essential mechanism of electrochemical doping process:<sup>16</sup>



As observed in this process, a proton is simultaneously encapsulated into the  $\text{TiO}_2$  lattice, combining with oxygen and forming  $\text{Ti}^{3+}$  species, which results in free electrons that in turn decrease the electrical resistance.

In terms of expanding the optical absorption range of  $\text{TiO}_2$ , numerous studies have been devoted to CdS-coupled  $\text{TiO}_2$ , due to its narrow band gap (2.24 eV) and suitable band alignment with  $\text{TiO}_2$ .<sup>17,18</sup> Significant improvement in incident photon-to-charge carrier generation efficiency (IPCE) was achieved on CdS-decorated  $\text{TiO}_2$  NTs, in comparison with the  $\text{TiO}_2$  nanoparticle counterpart. Considering the aspects of the electrical conductivity and visible light response, we propose in this work, for the first time, the construction of CdS-sensitized reduced  $\text{TiO}_2$  NTs through electrochemical doping process. Enhanced photoelectrochemical activity should be expected.

## Results and discussion

### Structural and optical characterization

Fig. 1 shows the surface morphology of the pristine  $\text{TiO}_2$  NTs, reduced  $\text{TiO}_2$  NTs and CdS-R- $\text{TiO}_2$  NTs. Compact and vertically aligned nanotube arrays were produced by the electrochemical anodization, with porous diameters around 100 nm and tube lengths *ca.* 3.7  $\mu\text{m}$  (Fig. 1a and b). The cathodic reduction does not dramatically change the tube structure, except that the tube walls become slightly thicker, and the inner porous diameter correspondingly decreases, as observed in Fig. 1c. Probably, owing to the shrinkage of the inner tube diameter, it becomes more difficult for  $\text{Cd}^{2+}$  and  $\text{S}^{2-}$  ions to spread into such tiny channels because of the strong capillary forces; thus, large aggregates of CdS particles are essentially deposited on the top surface of the R- $\text{TiO}_2$  NTs (Fig. 1d).

To provide evidence for crystalline phase identification, X-ray diffraction patterns of the prepared samples were recorded and are shown in Fig. 2. The presence of diffraction peaks at  $25.5^\circ$ ,  $37.9^\circ$ ,  $48.3^\circ$  and  $53.9^\circ$  strongly support the predominant formation of anatase  $\text{TiO}_2$  after the annealing process. These diffraction peaks are associated with the (101), (004), (200) and (105) planes of anatase, respectively.<sup>16</sup> In addition, few peaks belonging to the titanium substrate are also detected, as shown in the pattern. The peak of titanium at  $38.5^\circ$  overlaps the anatase (004) plane, which intensifies that peak. For R- $\text{TiO}_2$  NTs, no shift in the diffraction peaks is observed; the only difference is that the peak intensities are slightly reduced. This suggests that the cathodic reduction has only a minor influence on the phase change of  $\text{TiO}_2$  NTs. As observed, for CdS-R- $\text{TiO}_2$  NTs the appearance of diffractive peaks located at  $26.6^\circ$  and  $52.5^\circ$  suggests the formation of a hexagonal CdS phase. Because the spread coverage of CdS aggregates on the top surface of the nanotube,

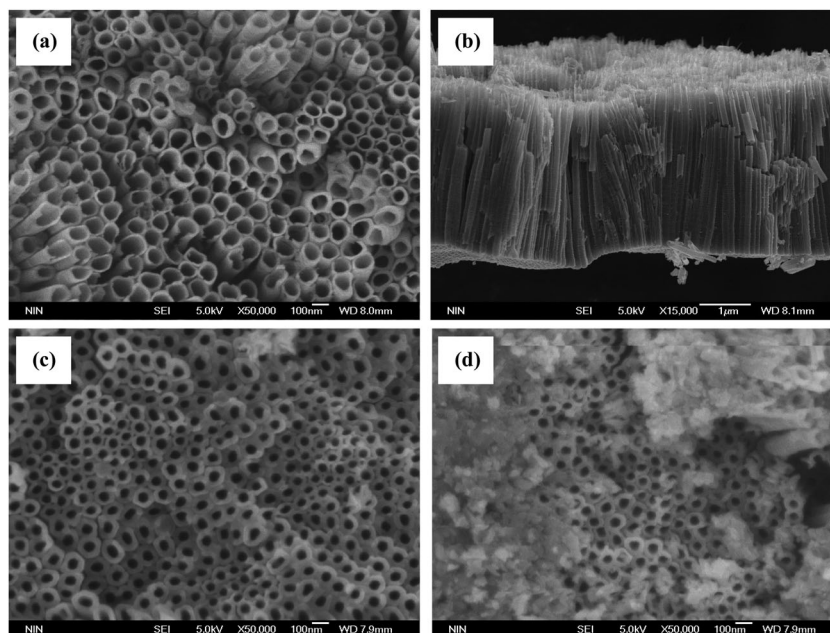


Fig. 1 Scanning electron microscopy images of pristine  $\text{TiO}_2$  NTs: (a) top view; and (b) cross-sectional view; (c) R- $\text{TiO}_2$  NTs and (d) CdS-R- $\text{TiO}_2$  NTs.

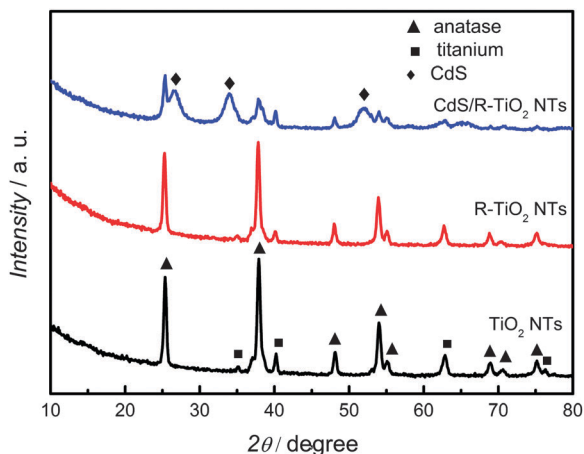


Fig. 2 XRD spectra of pristine  $\text{TiO}_2$  NTs, R- $\text{TiO}_2$  NTs and CdS-R- $\text{TiO}_2$  NTs.

as revealed in Fig. 1d, the peak intensities of  $\text{TiO}_2$  are slightly compromised.

Raman spectroscopy was performed to further identify the composite structure, as displayed in Fig. 3. For the pristine  $\text{TiO}_2$  NTs, the characteristic peaks at  $145\text{ cm}^{-1}$ ,  $395.9\text{ cm}^{-1}$ ,  $518.8\text{ cm}^{-1}$  and  $639.4\text{ cm}^{-1}$  justify the existence of an anatase phase. In comparison, the peak positions of R- $\text{TiO}_2$  NTs are slightly shifted, suggesting the change in the interactions between the laser and the molecule vibrational modes.<sup>19,20</sup> This could be associated with the alteration of Ti-O chemical bond type and an electron cloud distribution change in the reduced  $\text{TiO}_2$  NTs lattice. For CdS-R- $\text{TiO}_2$  NTs, the additional peaks at  $309.2\text{ cm}^{-1}$  and  $603.5\text{ cm}^{-1}$  confirm the deposition of CdS nanoparticles.

XPS measurements were further conducted to analyze the elemental composition and the chemical state of the synthesized materials. The general survey spectrum of CdS-R- $\text{TiO}_2$  NTs is shown in the Fig. S1 (ESI<sup>†</sup>), where Cd, S, Ti, O, N and C elemental peaks can be observed. The possible sources of carbon and nitrogen result from contamination during the sample handling and preparation processes. High resolution XPS spectra of O 1s

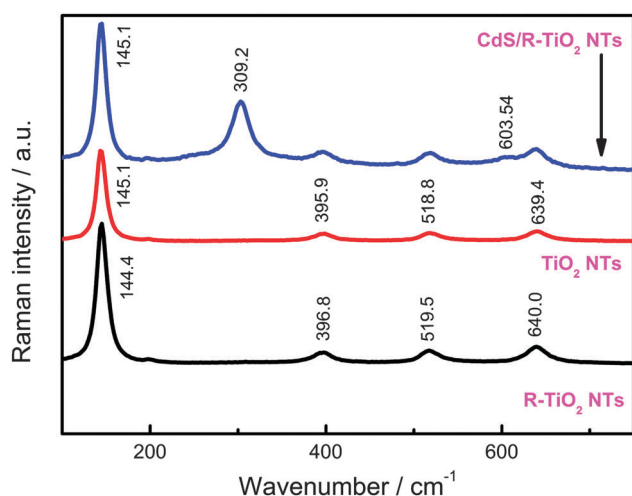


Fig. 3 Raman spectra of pristine  $\text{TiO}_2$  NTs, R- $\text{TiO}_2$  NTs and CdS-R- $\text{TiO}_2$  NTs.

and Ti 2p orbitals were obtained (Fig. 4) to reveal the chemical states in the pristine  $\text{TiO}_2$  NTs and R- $\text{TiO}_2$  NTs samples. As observed, two broad peaks with binding energies of 458.40 and 464.12 eV are close to the standard  $\text{Ti } 2p_{3/2}$  and  $\text{Ti } 2p_{1/2}$  orbital values in  $\text{TiO}_2$  NTs, and the splitting energy of 5.7 eV further suggests the presence of  $\text{Ti}^{4+}$  species.<sup>13</sup> Slight shifting of the

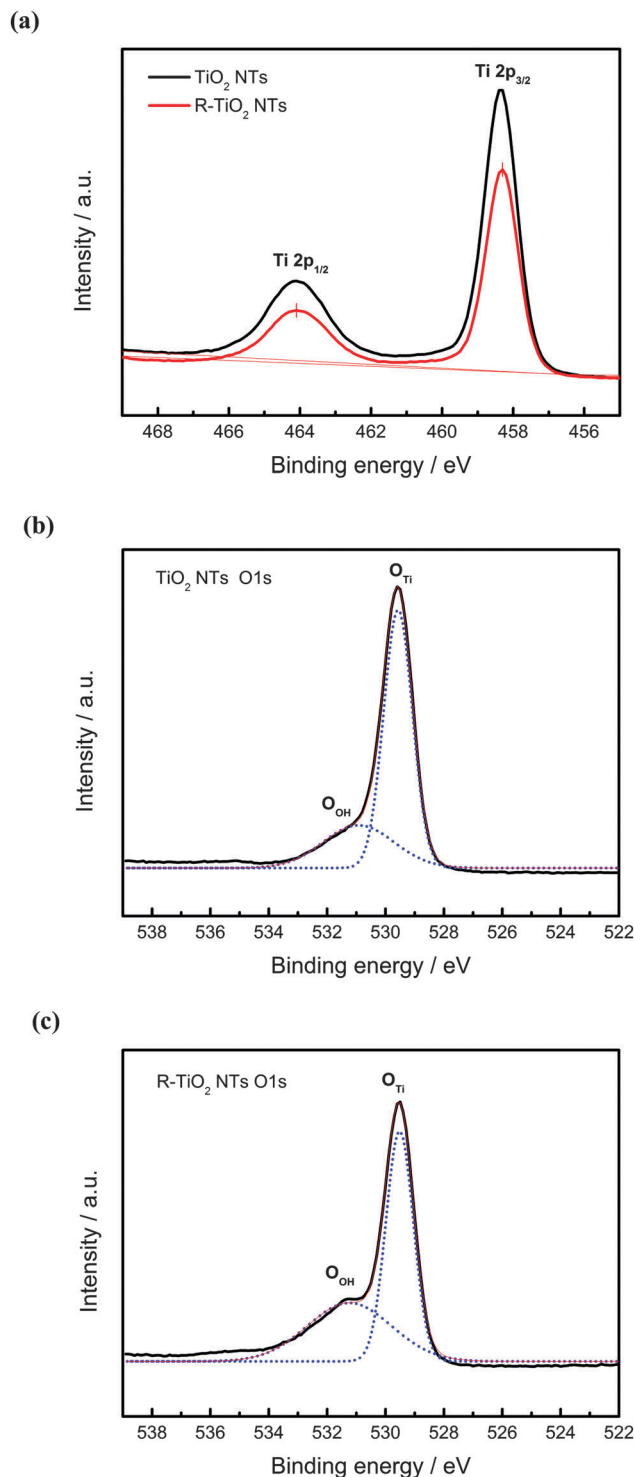


Fig. 4 XPS spectra of Ti 2p orbital (a); O 1s in  $\text{TiO}_2$  NTs (b); and O 1s in R- $\text{TiO}_2$  NTs (c).

peaks towards lower binding energy is observed in R-TiO<sub>2</sub> NTs, suggesting the presence of a lower valence state. It seems that the above-mentioned evidence is not strong enough to support the formation of Ti<sup>3+</sup> species, whereas previous works demonstrate the actual occurrence of Ti<sup>4+</sup> reduction to Ti<sup>3+</sup> at potentials around −0.95 V vs. Ag/AgCl in neutral electrolytes.<sup>21,22</sup> It is assumed that the disappearance of the Ti<sup>3+</sup> peak could be attributed to its sensitivity to oxidize in air. As the surface Ti<sup>3+</sup> is susceptible to be oxidized rather than the bulk Ti<sup>3+</sup>, it becomes difficult for the XPS technique to capture the feature because the resolution depth is only about 2.1 nm.<sup>11</sup>

Further, the O 1s orbitals in both the samples were scanned, from which two separate peaks centered at 529.5 and 530.9 eV can be split with one attributed to titanium-bonded oxygen (Ti–O) and another to hydrogen-bonded oxygen (O–H). No substantial change in peak positions can be observed, whereas the relative peak area of O<sub>Ti</sub>:O<sub>OH</sub> between pristine TiO<sub>2</sub> NTs and R-TiO<sub>2</sub> NTs show a pronounced variation. Because the atom ratio can be quantified by the relative peak area, the atom percentage of O<sub>OH</sub> (atom<sub>OH</sub>%) and O<sub>Ti</sub> (atom<sub>O–Ti</sub>%) change before and after the reduction of TiO<sub>2</sub> NTs were calculated<sup>23</sup> (listed in Table 1). It is observed that the atom<sub>OH</sub>% shows a dramatic increase from 28.93% to 43.70% after TiO<sub>2</sub> NTs reduction; on the contrary, the atom<sub>Ti</sub>% drops from 71.07% to 56.29%. Therefore, the variation of lattice oxygen to hydroxyl oxygen ratio helps to confirm the H<sup>+</sup> intercalation and Ti<sup>3+</sup> formation.<sup>24</sup>

Fig. 5 compares the optical absorption properties of the synthesized materials in the UV-visible light region. It is noted in Fig. 5a that the reduced TiO<sub>2</sub> NTs show considerably stronger UV absorption intensity than the bare TiO<sub>2</sub> NTs, whereas the absorption edge slightly shifts to a lower wavelength. The addition of CdS on R-TiO<sub>2</sub> NTs results in considerably broader and stronger absorption in the UV-visible region. By applying the following equation,<sup>25</sup> the band gap of these samples are calculated:

$$(\alpha h\nu)^2 = C(h\nu - E_g)$$

where  $\alpha$  is the absorption coefficient;  $h$  is Planck's constant;  $\nu$  is the light vibration frequency;  $C$  is a proportional constant; and  $E_g$  is the band gap. The absorbance value  $A$  obtained from the UV-vis DRs spectrum is proportional to the absorption coefficient  $\alpha$ ; thus, the band gap value is deduced by plotting  $(Ah\nu)^2$

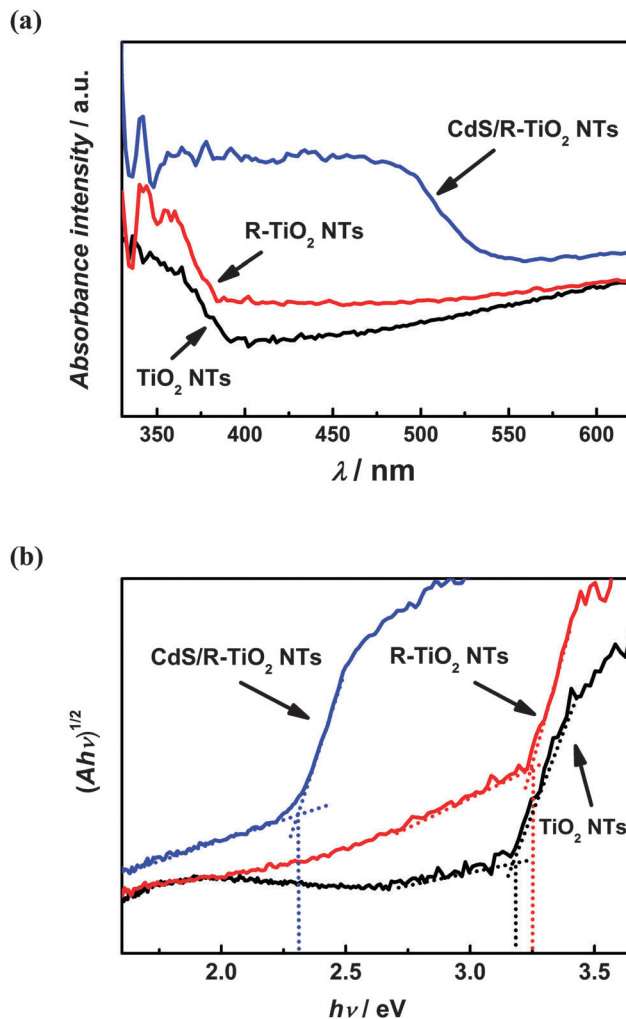


Fig. 5 UV-vis diffuse reflectance spectra of pristine TiO<sub>2</sub> NTs, R-TiO<sub>2</sub> NTs and CdS–R-TiO<sub>2</sub> NTs (a); plots of band gap of pristine TiO<sub>2</sub> NTs, R-TiO<sub>2</sub> NTs and CdS–R-TiO<sub>2</sub> NTs (b).

against the photon energy  $h\nu$  and extrapolating the intersection point of the linear part and background with the horizontal axis. It can be seen in Fig. 5b that the band gap is increased for R-TiO<sub>2</sub> NTs, which is inconsistent with the previous theory.<sup>10,13</sup> According to literatures,<sup>26–28</sup> the phenomenon of band gap broadening as found in this work, also known as Burstein–Moss shift, is observed in some degenerate semiconductors,

Table 1 O<sub>OH</sub> and O<sub>Ti</sub> percentage determined from high resolution XPS spectra

Sample/orbitals	Orbitals	Peak position/eV	Peak area	Atom <sub>OH</sub> (%)	Atom <sub>O–Ti</sub> (%)
TiO <sub>2</sub> NTs O 1s	O <sub>Ti</sub>	529.57	121643.61	28.93	71.07
	O <sub>OH</sub>	530.92	49515.15		
R-TiO <sub>2</sub> NTs O 1s	O <sub>Ti</sub>	529.52	81677.04	43.70	56.29
	O <sub>OH</sub>	531.24	63404.97		
TiO <sub>2</sub> NTs Ti 2p	Ti 2p <sub>1/2</sub>	458.40	—	—	—
	Ti 2p <sub>3/2</sub>	464.12	—		
R-TiO <sub>2</sub> NTs Ti 2p	Ti 2p <sub>1/2</sub>	458.33	—	—	—
	Ti 2p <sub>3/2</sub>	464.08	—		



in which the electron carrier concentration is extremely high. When the states close to the conduction band edge are all populated with electrons, the Fermi level is pushed towards higher energy. Therefore, more energy is required to excite the electrons from the valence band top into the conduction band above the Fermi level, leading to the occurrence of a Burstein–Moss shift. In this study, the cathodic polarization of  $\text{TiO}_2$  NTs was performed at  $-1.5$  V for 20 min, which is considerably longer than the time required for conductivity to switch on.<sup>21,22</sup> Thus, such a long time reduction brought about an increased number of charge carriers, reinforced the scattering effect and a broader band gap. All these competitive factors will eventually determine the overall conductivity of R- $\text{TiO}_2$  NTs. As a narrow band gap semiconductor, CdS nanoparticles substantially bring about a band gap decrease to about 2.3 eV, as shown in Fig. 5b. From these spectral features, it is concluded that the composite CdS-R- $\text{TiO}_2$  NTs possess excellent UV-visible response and high charge carrier concentration.

### Electrochemical studies

Fig. 6 compares the cyclic voltammograms of  $\text{TiO}_2$  NTs recorded at a scan rate of  $100 \text{ mV s}^{-1}$  in  $0.1 \text{ M Na}_2\text{SO}_4$ , before and after the cathodic reduction at  $-1.5$  V vs. Ag/AgCl. From the curves it can be observed that the pristine  $\text{TiO}_2$  NTs show the characteristic response: the cathodic current exponentially increases towards the negative potentials, and negligible capacitive current flows in the positive potential range. By contrast, R- $\text{TiO}_2$  NTs show a significant capacitive current increase in the positive potential range. This is another piece of evidence that proton intercalation indeed happens and that it induces the formation of shallow band gap states below the conduction band of  $\text{TiO}_2$ .<sup>15,28</sup> The population of electrons into the conduction band from the shallow states could easily proceed at room temperature; thus, a large current flow is observed. From the chemical perspective, the combination of proton with oxygen decreases the number of lattice oxygen, thereby impairing the binding

force of electrons to titanium atoms and subsequently leading to the facile movement of electrons in the entire material. Accompanied by this process is the visual change of  $\text{TiO}_2$  color from grey into dark blue, as shown in the inset images in Fig. 6. This phenomenon is often regarded as the filling of electrons in the sub-band gap states, with an elevation of Fermi level in  $\text{TiO}_2$ .

The electrical properties of  $\text{TiO}_2$  NTs after the cathodic reduction were further investigated by the electrochemical impedance spectroscopy as shown in Fig. 7. As observed both in the dark and under illumination, the reduced  $\text{TiO}_2$  NTs exhibit dramatically decreased resistance compared with the pristine  $\text{TiO}_2$  NTs. For the pristine  $\text{TiO}_2$  NTs in the dark, the simple RC equivalent circuit can explain the Nyquist plot, whereas for the R- $\text{TiO}_2$  NTs, the high frequency part exhibits a  $45^\circ$  line followed by a low frequency arc, which fits the transmission line behavior.<sup>29</sup> The transmission line model (shown in Fig. S3, ESI†), which incorporates the transport resistance, the charge transfer resistance at the solid/liquid interface along the

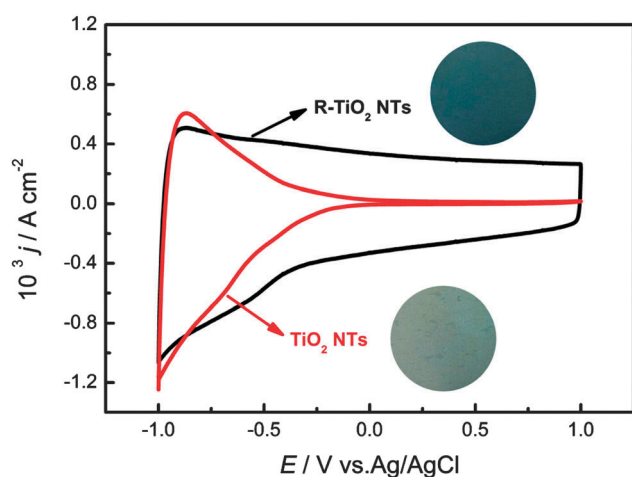


Fig. 6 Cyclic voltammograms of  $\text{TiO}_2$  NTs and R- $\text{TiO}_2$  NTs in  $0.1 \text{ M Na}_2\text{SO}_4$  recorded at a scan rate of  $100 \text{ mV s}^{-1}$ . The inset shows the color change of  $\text{TiO}_2$  NTs after the cathodic reduction.

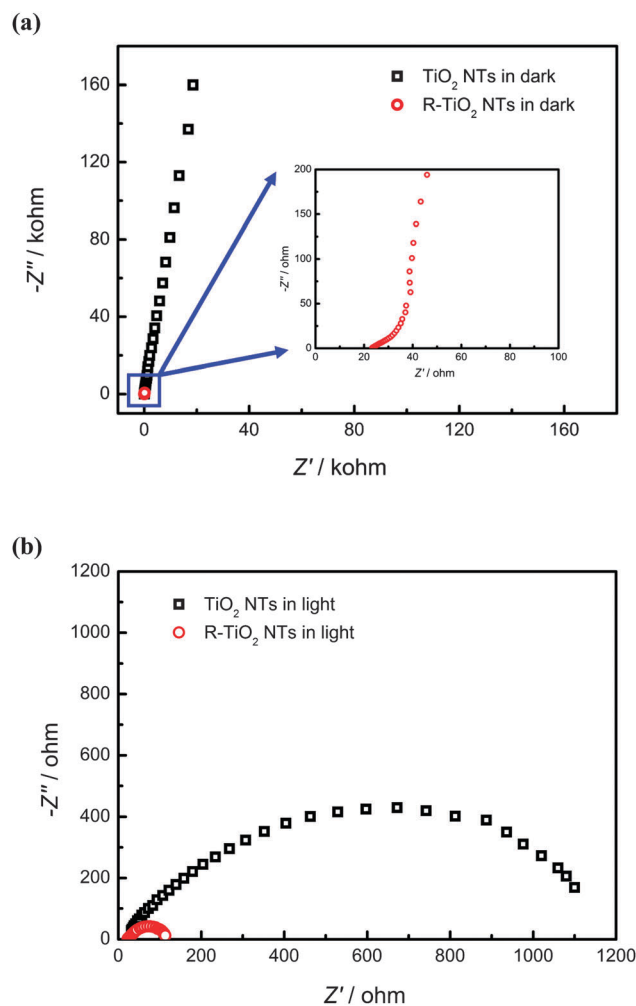


Fig. 7 Nyquist plots of  $\text{TiO}_2$  NTs before and after the cathodic reduction in the dark (a) and under illumination (b). Spectra were recorded in the range of 1 to 1000 Hz at a modulation frequency of 10 mV in  $0.1 \text{ M Na}_2\text{SO}_4$  electrolyte.

Table 2 Fitted equivalent circuit elements from the impedance spectra<sup>a</sup>

Conditions	Sample	$R_s$ ( $\Omega$ cm <sup>-2</sup> )	$R_{ct}$ ( $\Omega$ cm <sup>-2</sup> )	$R_{tr}$ ( $\Omega$ cm <sup>-2</sup> )	CPE (F cm <sup>-2</sup> )	$n$
In the dark	TiO <sub>2</sub> NTs	21.91	$4.94 \times 10^6$	—	$7.69 \times 10^{-6}$	0.93
	R-TiO <sub>2</sub> NTs	20.07	—	25.74	$1.44 \times 10^{-3}$	0.93
Under illumination	TiO <sub>2</sub> NTs	18.29	1246	—	$4.73 \times 10^{-5}$	0.74
	R-TiO <sub>2</sub> NTs	27.6	90.79	—	$2.25 \times 10^{-3}$	0.92

<sup>a</sup>  $R_s$  represents solution resistance;  $R_{ct}$  represents charge transfer resistance;  $R_{tr}$  represents charge transport resistance, and CPE is the constant phase element ( $n$  is an exponential term).

transport channel, and the total capacitance including the solid phase and solid/liquid interface, is often employed to describe the impedance behavior of the nanoporous metal oxide electrodes.

On the basis of the proposed equivalent circuits, the circuit elements were derived and are shown in Table 2. The constant phase element (CPE) was used to replace the capacitance when  $n$  is between 0.9 and 1 due to the inhomogeneous surface on nanoporous electrodes.<sup>30</sup> It is worth noting that the capacitance is considerably enhanced (1000 times higher) for reduced TiO<sub>2</sub> NTs. This is consistent with the cyclic voltammetry results. The enhanced capacitance is most likely attributed to, according to the literature, the formation of depletion zone at nanotube wall surface that arises from the multiple donor states after H<sup>+</sup> intercalation.<sup>24</sup>

Under supra-band gap illumination, TiO<sub>2</sub> NTs can be excited and produce electrons and holes for surface reactions. Therefore, in Fig. 7b, the charge transfer semicircle appears for both the pristine and reduced TiO<sub>2</sub> NTs. The R-TiO<sub>2</sub> NTs exhibit a considerably smaller semicircle than the pristine TiO<sub>2</sub> NTs, indicating that the charge transfer proceeds more easily on the former electrode. The charge transfer resistance was derived by fitting the Nyquist plot with the Randles model; the results are shown in Table 2. As seen, the charge transfer resistance is highly decreased from 1246  $\Omega$  to 90.79  $\Omega$  cm<sup>-2</sup>; moreover, the capacitance increases nearly 100 times. The impedance result demonstrates that the competition between increased charge carrier concentration and the increased electron scattering leads to the overall enhanced conductivity that occurred after the TiO<sub>2</sub> NTs was electrochemically reduced. Therefore, improved capacitance and charge transfer across the interface is realized. The similar conclusion was drawn by a previous study, by performing Mott-Schottky measurements, the carrier density showed 5 orders of magnitude enhancement after the reduction treatment.<sup>31</sup> That is primarily owing to the deficiency of lattice oxygen induced by the H<sup>+</sup> intercalation. Moreover, the improved conductivity substantially contributes to the photocatalytic activity of R-TiO<sub>2</sub> NTs on salicylic acid degradation (shown in Fig. S3, ESI<sup>†</sup>), which illustrates the significance of charge carrier increase.

### Photoelectrochemical studies

Fig. 8a shows the photocurrent of CdS-R-TiO<sub>2</sub> NTs in 1 M Na<sub>2</sub>SO<sub>3</sub> electrolyte and the comparison with CdS-TiO<sub>2</sub> NTs. Notably, the CdS-R-TiO<sub>2</sub> NTs sample presents an extremely

high photocurrent at saturation around 26.6 mA cm<sup>-2</sup>, which is almost twice higher than that of CdS-TiO<sub>2</sub> NTs (13.9 mA cm<sup>-2</sup>). In addition, the photocurrent onset potential shifts to a strong negative value around -1.0 V, indicating the significant Fermi level rise after CdS deposition. As a consequence, the photocurrent reaches saturation at 0.0 V where the band bending is maximum and no recombination occurs. The  $j$ - $t$  curve shown in Fig. 8b indicates that the composite CdS-R-TiO<sub>2</sub> NTs possess excellent photo-response upon illumination and remain comparatively stable. This should be attributed to the superb hole scavenger ability of SO<sub>3</sub><sup>2-</sup> ions that capture holes, minimize recombination and stabilize CdS from photo-corrosion effectively.<sup>32</sup> The IPCE value of CdS-R-TiO<sub>2</sub> NTs calculated from the following equation is approximately 30.12%, which is twice higher than that of CdS-TiO<sub>2</sub> NTs:

$$\text{IPCE} = \frac{1240 \times I_{sc}}{\lambda \times P}$$

where  $I_{sc}$  represents the short circuit current density, mA cm<sup>-2</sup>;  $\lambda$  is the excitation light wavelength, nm; and  $P$  is the illumination power density, mW cm<sup>-2</sup>. In comparison, R-TiO<sub>2</sub> NTs do not produce any marked photocurrent under illumination, which is easy to understand because of the wide band gap of 3.2 eV. Therefore, the contribution of conductivity enhancement to photocurrent generation is verified by measuring the  $j$ - $t$  curves of TiO<sub>2</sub> NTs and R-TiO<sub>2</sub> NTs under UV irradiation (see Fig. 8c). As observed, the photocurrent of R-TiO<sub>2</sub> NTs increases by 33.3%, compared with that of TiO<sub>2</sub> NTs.

The photocurrent results further demonstrate the contribution of conductivity improvement in the solar conversion process. By introducing lattice oxygen vacancies (Ti<sup>3+</sup>) into TiO<sub>2</sub> NTs, shallow donor states are formed and more electrons are populated into the conduction band. This facilitates the increased number of charge carriers to be collected and participate in surface reactions. The present investigation allows us to take electrical conductivity in nano-structures into serious consideration when devising new materials for solar conversion.

Finally, the stability of CdS-R-TiO<sub>2</sub> NTs composite was considered, and measured under constant illumination for 6000 s (shown in Fig. 9). It is observed that the photocurrent shows a gradual decay over the process and reaches 17.5 mA cm<sup>-2</sup> at the end. It is calculated that the photocurrent actually decreases by 30% for 6000 s illumination. The drop in photocurrent density could be because of the CdS dissolution as the hole scavenger is depleted over time, or conductivity loss of R-TiO<sub>2</sub> NTs under

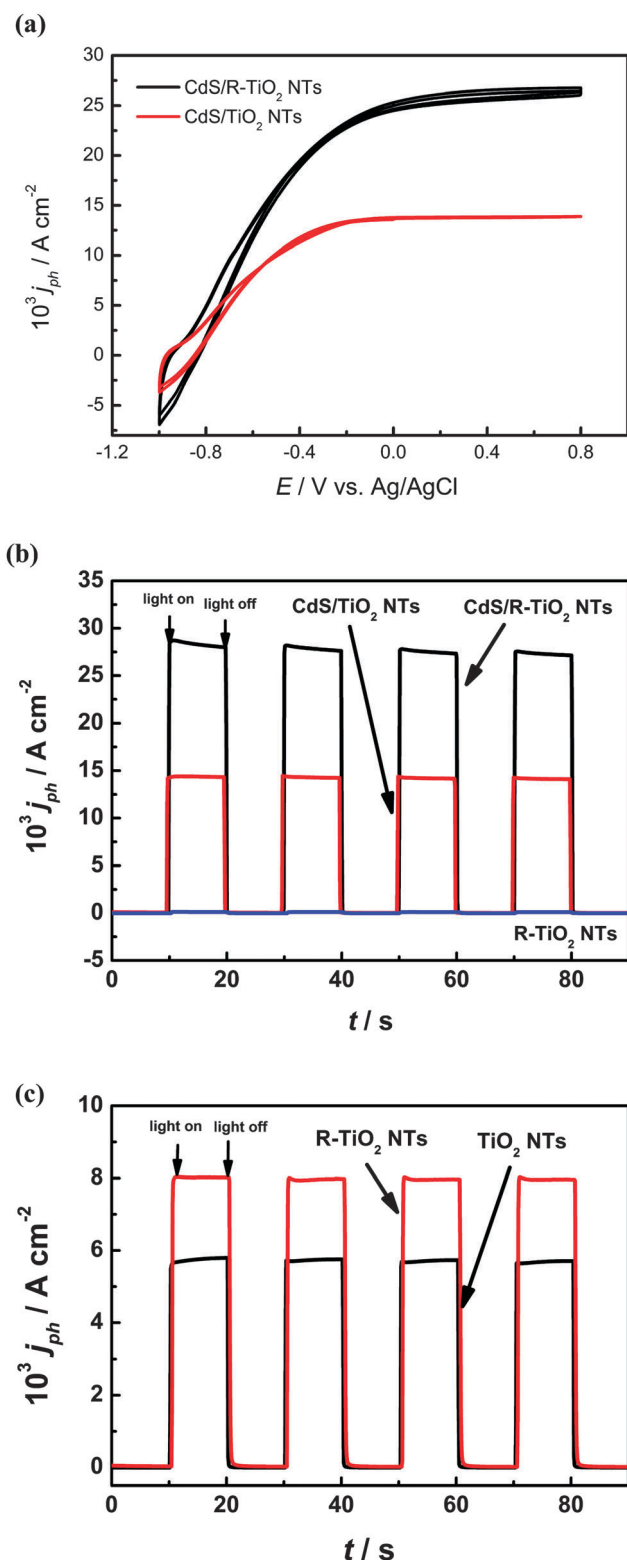


Fig. 8 Photocurrent responses: (a)  $j$ - $V$  curves of CdS-R-TiO<sub>2</sub> NTs and CdS-TiO<sub>2</sub> NTs recorded at a scan rate of 100 mV s<sup>-1</sup> under photo-stationary conditions; (b) transient  $j$ - $t$  curves of CdS-R-TiO<sub>2</sub> NTs and CdS-TiO<sub>2</sub> NTs recorded at 0.2 V, in 1 M Na<sub>2</sub>SO<sub>3</sub> electrolyte under irradiation of 420 nm light at power density of 247.9 mW cm<sup>-2</sup>; (c) transient  $j$ - $t$  curves of R-TiO<sub>2</sub> NTs and TiO<sub>2</sub> NTs recorded at 0.5 V, in 0.1 M Na<sub>2</sub>SO<sub>4</sub> electrolyte under irradiation of 375 nm light at power density of 300.0 mW cm<sup>-2</sup>.

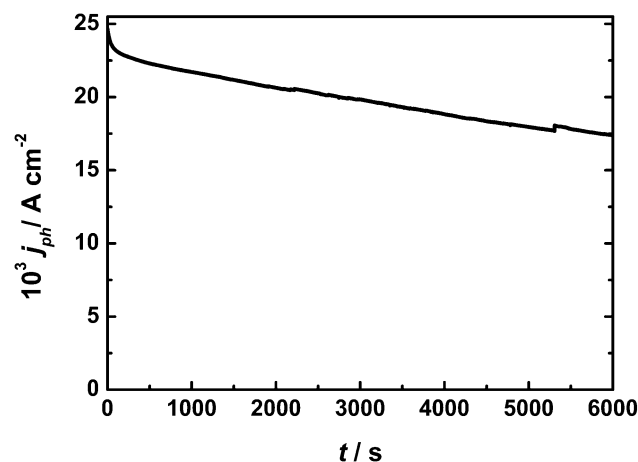


Fig. 9 Photocurrent change profile of CdS-R-TiO<sub>2</sub> NTs at 0.2 V in 1 M Na<sub>2</sub>SO<sub>3</sub> electrolyte under irradiation of 420 nm light at power density of 247.9 mW cm<sup>-2</sup>.

positive bias. Therefore, further studies are conducted to address the problem of stability of the CdS-R-TiO<sub>2</sub> NTs.

## Conclusions

To conclude, CdS-decorated reduced TiO<sub>2</sub> NTs has been successfully synthesized and thoroughly characterized. The band gap broadening of R-TiO<sub>2</sub> NTs observed from the UV-vis spectrum suggests the increased electron concentration. A substantial decrease in charge transport and interfacial charge transfer resistance are found for R-TiO<sub>2</sub> NTs. The introduction of lattice oxygen vacancies (Ti<sup>3+</sup>) during the reduction process, as evidenced by the XPS results, can account for the improved conductivity and charge transport properties of TiO<sub>2</sub> NTs. Combined with the contribution from CdS that extended the light absorption into visible region, such enhancement brought about the significant increase in photocurrent densities (26.6 mA cm<sup>-2</sup>) for CdS-R-TiO<sub>2</sub> NTs, which is nearly twice higher than that of conventional CdS-TiO<sub>2</sub> NTs. The results uncovered in this work further illustrate the importance of the charge transport in the light conversion process and point out a promising route for material modification in solar light utilization and conversion fields.

## Experimental section

### Preparation of CdS-R-TiO<sub>2</sub> NTs

TiO<sub>2</sub> NTs was prepared by the electrochemical anodization at constant potentials. Prior to that, the titanium sheet was cut into pieces with dimension of 2 × 4 cm<sup>2</sup>, immersed in an aqua-regia for 24 h and ultrasonically cleaned in absolute ethanol for 15 min to remove surface grease and dirt. Then, the pretreated titanium substrate served as the working electrode and platinum as the counter one, both of which were immersed in the electrolyte comprising 0.3 wt% NH<sub>4</sub>F, 3 vol% H<sub>2</sub>O and ethylene glycol. A constant potential of 50 V was applied to the electrodes for 1 h, to induce the *in situ* growth of TiO<sub>2</sub> NTs from the Ti substrate.

The as-prepared TiO<sub>2</sub> NT samples were amorphous structures; thus, a high temperature annealing at 500 °C is performed in ambient atmosphere for 2 h, with temperature ramp of 1 °C min<sup>-1</sup> to induce crystallization.

The electrochemical doping *via* cathodic polarization produces the reduced TiO<sub>2</sub> NTs (denoted as R-TiO<sub>2</sub> NTs). The external potential was provided by a CHI 660D potentiostat. The experiment was performed in one compartment cell with three-electrode configuration, employing TiO<sub>2</sub> NTs as the working electrode, Pt as auxiliary and Ag/AgCl (3 M KCl) as reference electrodes. The supporting electrolyte was 0.1 M Na<sub>2</sub>SO<sub>4</sub>. The reduction was performed at constant -1.5 V *vs.* Ag/AgCl for a period of 20 min to obtain the R-TiO<sub>2</sub> NTs samples.

Finally, CdS nanoparticles were deposited on the top of the R-TiO<sub>2</sub> NTs through the successive ionic layer adsorption and reaction (SILAR) method. Typically, the R-TiO<sub>2</sub> NTs sample was sequentially immersed in 0.05 M Cd(Ac)<sub>2</sub>, D.I. water, 0.05 M Na<sub>2</sub>S and D.I. water for 1 min each with magnetic stirring. This is called one SILAR cycle. The process was repeated 9 times to ensure the uniform coverage of CdS, and then the composite was thoroughly rinsed with D.I. water and dried at 60 °C for 40 min. For comparison, CdS sensitized TiO<sub>2</sub> NTs were also prepared with the same deposition cycles and amount. All the chemicals used in this work were of analytical grade and used without further purification.

### Material characterization

Scanning electron microscopy (SEM) was performed on a JEOL JSM-6700F instrument (Japan). X-ray diffraction patterns were obtained from an X'pert PRO MRD diffractometer using a Cu-K<sub>α</sub> source ( $\lambda = 0.15416$  nm), with scanning angle ( $2\theta$ ) range from 10 to 80°. UV-vis diffuse reflectance spectroscopy was conducted on a Hitachi U-4100 spectrophotometer with scanning wavelength range 300–800 nm, using Ba<sub>2</sub>SO<sub>4</sub> as reference. Raman spectra were obtained on the HR 800 laser Raman spectrometer (Horiba Jobin Yvon, France), with the Ar<sup>+</sup> laser (20 mW) as the excitation source. The valence state of TiO<sub>2</sub> NTs before and after the cathodic reduction was analyzed by the X-ray photoelectron spectrometry (XPS) on AXIS Ultra DLD instrument (Al K<sub>α</sub> irradiation;  $h\nu = 1486.71$  eV). The XPS data were calibrated using the binding energy of C 1s (284.6 eV) as the standard.

### Electrochemical and photoelectrochemical studies

The electrochemical properties of TiO<sub>2</sub> NTs before and after the cathodic reduction were investigated by cyclic voltammetry and impedance spectroscopy on a CHI 660D potentiostat. The conventional three-electrode configuration, in which the prepared TiO<sub>2</sub> NTs or R-TiO<sub>2</sub> NTs as working electrode, platinum as counter and Ag/AgCl (3 M KCl) as reference electrodes, was employed. Na<sub>2</sub>SO<sub>4</sub> aqueous solution (0.1 M) was used as the supporting electrolyte. The scanning potential range was -1.0 to 1.0 V, at a scan rate of 100 mV s<sup>-1</sup>. The impedance measurements were conducted under DC potential of 0.5 V both in the dark and under illumination, in order to compare the electronic conductivity of TiO<sub>2</sub> NTs and R-TiO<sub>2</sub> NTs. The excitation light source was provided by a 375 nm LED at power

intensity of 150 mW cm<sup>-2</sup>. Spectra were recorded in the range of 0.1 to 1000 Hz at sinusoidal modulation amplitude of 10 mV rms.

The photocurrent *vs.* potential curves and transient photocurrent spectroscopy were measured over CdS-R-TiO<sub>2</sub> NTs electrodes. The experiments were conducted in a home-built quartz cell with the same electrode configuration as the dark electrochemistry. The CdS-R-TiO<sub>2</sub> NTs electrode, with geometric area of 1 cm<sup>2</sup> immersing in 1 M Na<sub>2</sub>SO<sub>3</sub> electrolyte, faces towards the flattened quartz window. The 420 nm LED light with optical power density of 247.9 mW cm<sup>-2</sup> was employed as the exciting light source. The photocurrent *vs.* time curve of R-TiO<sub>2</sub> NTs was measured in 0.1 M Na<sub>2</sub>SO<sub>4</sub> electrolyte, under illumination of 375 nm LED light at 300 mW cm<sup>-2</sup>. The photoelectrocatalytic activity of R-TiO<sub>2</sub> NTs was also evaluated by the decomposition of salicylic acid. For more experimental details, please see the ESI.†

## Acknowledgements

The authors gratefully acknowledge the financial support from National Natural Science Foundation of China (Grant No. 21307098), China Postdoctoral Science Foundation (2013M532053), and the Fundamental Research Funds for the Central Universities of China. Special thanks are given to technician Zhuang Miao in Northwest Institute for Non-ferrous Metal Research for kind help in SEM images, and technician Penghui Guo in the State Key Laboratory of Multiphase Flow in Power Engineering for XPS spectra.

## References

- 1 A. Fujishima, *Nature*, 1972, **238**, 37.
- 2 P. Docampo, S. Guldin, U. Steiner and H. J. Snaith, *J. Phys. Chem. Lett.*, 2013, **4**, 698.
- 3 D. Gong, C. A. Grimes, O. K. Varghese, W. Hu, R. Singh, Z. Chen and E. C. Dickey, *J. Mater. Res.*, 2001, **16**, 3331.
- 4 K. Zhu, N. R. Neale, A. Miedaner and A. J. Frank, *Nano Lett.*, 2007, **7**, 69.
- 5 A. Lamberti, A. Sacco, S. Bianco, D. Manfredi, F. Cappelluti, S. Hernandez, M. Quaglio and C. F. Pirri, *Phys. Chem. Chem. Phys.*, 2013, **15**, 2596.
- 6 C. Richter and C. A. Schmuttenmaer, *Nat. Nanotechnol.*, 2010, **5**, 769.
- 7 Q. Zhang, V. Celorrio, K. Bradley, F. Eisner, D. Cherns, W. Yan and D. J. Fermin, *J. Phys. Chem. C*, 2014, **118**, 18207–18213.
- 8 R. P. Lynch, A. Ghicov and P. Schmuki, *J. Electrochem. Soc.*, 2010, **157**, G76.
- 9 F. Fabregat-Santiago, I. Mora-Sero, G. Garcia-Belmonte and J. Bisquert, *J. Phys. Chem. B*, 2003, **107**, 758.
- 10 F. Zuo, L. Wang, T. Wu, Z. Zhang, D. Borchardt and P. Feng, *J. Am. Chem. Soc.*, 2010, **132**, 11856.
- 11 S. Tominaka, Y. Tsujimoto, Y. Matsushita and K. Yamaura, *Angew. Chem., Int. Ed.*, 2011, **50**, 7418.
- 12 X. Zhang, H. Tian, X. Wang, G. Xue, Z. Tian, J. Zhang, S. Yuan, T. Yu and Z. Zou, *Mater. Lett.*, 2013, **100**, 51.



- 13 Q. Kang, J. Cao, Y. Zhang, L. Liu, H. Xu and J. Ye, *J. Mater. Chem. A*, 2013, **1**, 5766.
- 14 M. Xing, W. Fang, M. Nasir, Y. Ma, J. Zhang and M. Anpo, *J. Catal.*, 2013, **297**, 236.
- 15 F. Fabregat-Santiago, E. M. Barea, J. Bisquert, G. K. Mor, K. Shankar and C. A. Grimes, *J. Am. Chem. Soc.*, 2008, **130**, 11312.
- 16 A. Fujishima, X. Zhang and D. A. Tryk, *Surf. Sci. Rep.*, 2008, **63**, 515.
- 17 W.-T. Sun, Y. Yu, H.-Y. Pan, X.-F. Gao, Q. Chen and L.-M. Peng, *J. Am. Chem. Soc.*, 2008, **130**, 1124.
- 18 Q. Zhang, H. Xu and W. Yan, *Electrochim. Acta*, 2012, **61**, 64.
- 19 H. Zhou and Y. Zhang, *J. Phys. Chem. C*, 2014, **118**, 5626.
- 20 W. Wei, N. Yaru, L. Chunhua and X. Zhongzi, *RSC Adv.*, 2012, **2**, 8286.
- 21 H. Zhou and Y. Zhang, *J. Power Sources*, 2013, **239**, 128.
- 22 J. M. Macak, B. G. Gong, M. Hueppe and P. Schmuki, *Adv. Mater.*, 2007, **19**, 3027.
- 23 B. H. Meekins and P. V. Kamat, *ACS Nano*, 2009, **3**, 3437.
- 24 S. Li, J. Qiu, M. Ling, F. Peng, B. Wood and S. Zhang, *ACS Appl. Mater. Interfaces*, 2013, **5**, 11129.
- 25 A. G. Muñoz, *Electrochim. Acta*, 2007, **52**, 4167.
- 26 G. Yang, W. Yan, Q. Zhang, S. Shen and S. Ding, *Nanoscale*, 2013, **5**, 12432.
- 27 A. Sarkar, S. Ghosh, S. Chaudhuri and A. K. Pal, *Thin Solid Films*, 1991, **204**, 255.
- 28 M. Grundmann, *The physics of semiconductors*, Springer, Berlin, 2006, vol. 19, p. 37.
- 29 A. F. Halverson, K. Zhu, P. T. Erslev, J. Y. Kim, N. R. Neale and A. J. Frank, *Nano Lett.*, 2012, **12**, 2112.
- 30 F. Fabregat-Santiago, G. Garcia-Belmonte, J. Bisquert, A. Zaban and P. Salvador, *J. Phys. Chem. B*, 2001, **106**, 334.
- 31 X. Wu, Y. Ling, L. Liu and Z. Huang, *J. Electrochem. Soc.*, 2009, **156**, K65.
- 32 D. J. Fermin, E. A. Ponomarev and L. M. Peter, *Electrochem. Soc. Proceedings*, 1997, vol. 97-20, p. 62.